FeNC Oxygen Reduction Electrocatalyst with High Utilisation Penta-coordinated sites

Jesús Barrio,[a,b±] Angus Pedersen,[a,b±] Saurav Ch. Sarma,[b] Alexander Bagger,[b] Mengjun Gong,[c] Silvia Favero, [b] Chang-Xin Zhao,[d] Ricardo Garcia-Serres,[e] Alain Y. Li,[b] Qiang Zhang,[d] Frédéric Jaouen,[f] Frédéric Maillard,[g] Anthony Kucernak,[c] Ifan E. L. Stephens,[a*] Maria-Magdalena Titirici[b*]

a. Department of Materials, Royal School of Mines, Imperial College London, SW7 2AZ London, UK
b. Department of Chemical Engineering, Imperial College London, SW7 2AZ, London, UK
c. Department of Chemistry, Molecular Sciences Research Hub, Imperial College London, White City Campus W12 0BZ London, UK
d. Department of Chemical Engineering, Tsinghua University, 1 Tsinghua Road, Beijing 100084, P.R. China
e. Université Grenoble Alpes, CNRS, CEA, IRIG, Laboratoire de Chimie et Biologie des Métaux,17 Rue Des Martyrs, 38000, Grenoble, France
f. ICGM, University of Montpellier, CNRS, ENSCM, 1919 route de Mende, 34293 Montpellier, France
g. Université Grenoble Alpes, Université Savoie Mont-Blanc, CNRS, Grenoble-INP, LEPMI, Grenoble 38000, France

Email: i.stephens@imperial.ac.uk, m.titirici@imperial.ac.uk.

Abstract

Atomic Fe in N-doped carbon (FeNC) electrocatalysts for oxygen (O_2) reduction at the cathode of proton exchange membrane fuel cells (PEMFCs) are the most promising alternative to platinum-group-metal catalysts. Despite recent progress on atomic FeNC O_2 reduction, their controlled synthesis and stability for practical applications remains challenging. A two-step synthesis approach has recently led to significant advances in terms of Fe-loading and mass activity; however, the Fe utilisation remains low owing to the difficulty of building scaffolds with sufficient porosity that electrochemically exposes the active sites. Herein, we addressed this issue by coordinating Fe in a highly porous nitrogen doped carbon support (~3295 $m^2\ g^{-1}$), prepared by pyrolysis of inexpensive 2,4,6-triaminopyrimidine and a Mg^{2+} salt active site template and porogen. Upon Fe coordination, a high electrochemical active site density of 2.54×10^{19} sites g_{FeNC}^{-1} and a record 52% FeN_x electrochemical utilisation based on *in situ* nitrite stripping was achieved. The Fe single atoms are characterised pre- and post-electrochemical accelerated stress testing by aberration-corrected high-angle annular dark field scanning transmission electron microscopy, showing no Fe clustering. Moreover, *ex situ* X-ray absorption spectroscopy and low-temperature Mössbauer spectroscopy suggest the presence of penta-coordinated Fe sites, which were further studied by density functional theory calculations.

Introduction

Fe single atoms in nitrogen-doped carbon supports (FeNC) have emerged during the last decades as a promising cheap and accessible alternative electrocatalyst to precious group metals (PGMs) in the cathode of low temperature proton exchange membrane fuel cells (PEMFCs). Since Jasinski identified Fe macrocycles as promising PGM-free catalysts,[1] plenty of research has been devoted to improve the activity and stability of iron based catalysts for PEMFC cathodes, whose performance nearly equals that of Pt/C in fuel cells.[2–6] One of the most common approaches to improve the catalytic performance of FeNC materials is to enhance their intrinsic catalytic activity by modulation of the local coordination environment, for example by creating dual metal atom catalysts[7,8] or introducing axial ligands. Different FeN_x active site axial ligands have been recently proposed following *in situ* Mössbauer, x-ray absorption spectroscopy, nuclear inelastic scattering or electron paramagnetic

resonance. [9,10] Some of them bearing close resemblance to biological systems,[11] such as N axially coordinated FeN_4 sites resembling heme.[12] However, spectroscopic discernibility is often challenging in these typically heterogeneous FeNC catalysts,[13] therefore experimental structure-activity correlations are hard to conclude. To overcome experimental limitations, the effect of O axial ligands on model FeNC systems has been calculated by density functional theory,[14,15] although the effect of other possible axial ligands on different Fe sites (pyridinic and pyrrolic) has not been fully considered.[16] Alternatively, to improve catalyst performance, the number of active sites can be increased, an approach which has shown significant progress in recent years.[17] To selectively form a high density of atomic Fe sites and avoid undesired Fe-induced carbothermal reduction, Fellinger and co-workers first identified that the high temperature pyrolytic step (800-1000ºC) should be decoupled from the Fe loading, by using a suitable N_x site template.[17–20]

The decoupled two-step synthetic approach to prepare FeNC O_2 reduction catalysts has led to remarkable progress; Mehmood *et al.* recently showed bulk FeN_x site density ($SD_{Mössbauer,}$, Eq. 1-2) up to 7.4×10^{20} sites g_{FeNC}^{-1}. The reported *in situ* nitrite stripping site density ($SD_{nitrite}$, Eq. 3) was high at 4.67×10^{19} sites g_{FeNC}^{-1}, although the electrochemical utilisation of the total Fe ($Utilisation_{Nitrite/ICP}$ Eq. 4) and FeN_x sites ($Utilisation_{Nitrite/Mössbauer}$, Eq. 5) were both only 6%.[18] They additionally calculated that surface (accessible) FeN_x site density is restricted to $\sim10^{21}$ sites g_{FeNC}^{-1}, meaning their bulk (inaccessible) FeN_x site density approached this limit, while there was plenty of scope to increase their surface FeN_x site density.[18] It should also be considered that, at such high site density, the turnover frequency (TOF) may be constrained by electrical conductivity due to the high N-content. Nevertheless, for comparison, 3 nm diameter Pt nanoparticles (typical of commercial Pt/C) are geometrically constrained to ~35% of Pt atoms exposed on the nanoparticle surface.[21] Additionally, in cathodes of PEMFC, the ratio of specific Pt surface area ($m^2\ g_{Pt}^{-1}$) to that of Pt catalyst ($m^2\ g_{Pt}^{-1}$) is in range of ~70-90%, depending on preparation. Therefore, the electrochemical utilisation of the total Pt content at the PEMFC cathode is expected to be ~25-32% for 3 nm Pt, [22] with Pt surface site density of 1.31×10^{21} sites g_{Pt}^{-1} (electrochemical surface areas of 100 $m^2\ g_{Pt}^{-1}$ in PEMFCs of 2.8 nm Pt nanoparticles).[18] This demonstrates improvements in accessible surface FeN_x active sites are required to compete with Pt/C site densities.

Reported FeNC cathode catalyst layers in PEMFCs often possess thicknesses of ~100 µm, where transport resistances severely limits practical operation.[23,24] Ideally thicknesses should not exceed ~10 µm to minimise debilitating mass transport.[25] This means the total possible FeN_x sites in PEMFCs are restricted in terms of both sites g_{FeNC}^{-1} and sites cm_{FeNC}^{-3}. Therefore, methods for maximising the electrochemical accessibility of Fe within FeN_x sites in FeNC catalysts are critical to their optimisation and competition with PGM catalysts. By doing so, such catalysts could finally exploit the described theoretical benefit of atomically dispersed active sites with 100% utilisation of the metal. Excellent gas accessibility of FeN_x sites has already reached 100% as determined by *ex situ* cryo CO sorption.[17] However, to date, there has been limited progress in maximising the ratio of electrochemically accessible active sites. For optimal electrochemical utilisation of FeN_x in PEMFC, the active site is best located at the triple phase boundary (carbon (e^-), ionomer (H^+), and O_2). A utilisation metric of FeN_x sites was first established in 2015,[26] and later the exemplary work of Wan *et al*.[27] identified mesoporosity was critical in achieving their record $Utilisation_{Nitrite/ICP}$ and $Utilisation_{Nitrite/Mössbauer}$ of 43% with their FeNC, although at low $SD_{nitrite}$ of 1.32×10^{19} sites g_{FeNC}^{-1}. They also found rapidly decreasing utilisation with increasing $SD_{nitrite}$.[27] Other rotating disc electrode-based studies show $Utilisation_{Nitrite/ICP}$ based on *in situ* nitrite stripping (typically 0.2 $mg_{FeNC}\ cm^{-2}$, ~5 µm thickness) often remain <10%.[28] Even lower electrochemical active site utilisation values

are expected in PEMFCs where the active sites are commonly embedded in a thick catalyst layer (4 mg_{FeNC} cm^{-2}, ~100 µm). To obtain maximum Fe utilisation, materials that display both defined Fe-N_x sites and a hierarchical porous structure that allows an efficient O_2 transport and ionomer coverage are highly sought after. Zeolitic imidazolate framework-8 (ZIF-8) has been widely explored as a suitable template for porous carbons for electrocatalysis owing to its stable Zn-N_4 template and high specific surface area.[29,30] However, ZIF-8 is an entirely microporous material, requiring a post-synthetic heat treatment step to either open up the pore structure using dicyanamide[18] or CVD,[17] or incorporating mesoporosity via harsh silica template etching.[27,31]

Herein, we describe a facile method to prepare FeNC materials with a record high FeN_x electrochemical utilisation by using a Mg^{2+} salt as an active site template and porogen, along with an alternative organic precursor, 2,4,6-Triaminopyrimidine (TAP) to prepare a highly porous N-doped carbon host for Fe coordination. TAP interacts efficiently with the water molecules of the hydrated Mg^{2+} salt and melts upon pyrolysis to enable an efficient polymerization and a homogeneous distribution of Mg throughout the material. Fe is subsequently coordinated in the available N pyridinic moieties within the high specific surface area nitrogen-doped carbon (~3295 m^2 g^{-1}) through low-temperature wet impregnation resulting in highly available FeN_x active sites. The polymerization pathway and growth of the prepared materials is thoroughly studied by means of thermo-gravimetric analysis coupled to mass spectrometry, solid-state nuclear magnetic resonance, and X-ray photoelectron spectroscopy amongst others. The atomic Fe dispersion is confirmed by scanning transmission electron microscopy and energy dispersive x-rays, while the active site structure is elucidated through X-ray absorption spectroscopy, electron paramagnetic resonance and low temperature Mössbauer spectroscopy, where the dominant FeN_x site is found to be penta-coordinated by an axial ligand. The performance of the catalysts for O_2 reduction is evaluated in acidic media with rotating disk electrode measurements, where a high site density, low turnover frequency, and high utilisation can be obtained from *in situ* nitrite stripping. Finally, density functional theory (DFT) is used to evaluate the influence of axial ligands on model FeN_4 pyridinic and pyrrolic sites O_2 reduction activity, where a large change in OH binding energy, and therefore activity, is observed for varying axial ligands compared to a plain FeN_4 site.

Experimental section

Synthetic procedures

2,4,6-triaminopyrimidine (97% Sigma Aldrich) and magnesium chloride hexahydrate (99% Sigma Aldrich) were ground with a pestle and mortar in a weight ratio of 1:8 and the mixture pyrolyzed in a ceramic crucible (filled 1/3rd with material) at 800-1000°C for one hour (at set temperature) under N_2 atmosphere (>99.998%, BOC) with 300 mL min^{-1} flowrate and 5°C min^{-1} heating rate. The materials were collected, ground to fine powder, and washed with 2 M HCl (prepared by dilution of fuming 37% HCl, Merck) overnight to remove remaining $MgCl_2$ and MgO species. After the washing process, the powders were filtered, rinsed thoroughly with distilled water, dried at 80 °C under vacuum and labelled as TAP *X* (Where *X* denotes the pyrolysis temperature).

$^{57}FeCl_2$ Preparation (for Mössbauer)

The iron precursor iron chloride $^{57}FeCl_2$ was firstly prepared. ^{57}Fe (250 mg, Iron-57, 99.9% purity with 95.5% ^{57}Fe, Cambridge Isotope Laboratories) was added into a 1:1 37% HCl (Analytical reagent grade, Fisher Chemical) and H_2O solution (50 mL), then reflux (115ºC) was performed for 3h until everything was dissolved. Finally, $^{57}FeCl_2$ was obtained after leaving solution evaporating under vacuum at 60 °C for 3 hours, then 80°C overnight and freeze drying overnight.

Fe coordination

Fe was coordinated in the nitrogen moieties of the prepared TAP materials employing a low-temperature wet impregnation method in methanol reflux.[19,32] In this process, 60 mg of TAP material was placed in a 250 mL round-bottom flask along with 75 mL MeOH (AnalaR NORMAPUR Reag. Ph. Eur., ACS, VWR) under vigorous stirring until a homogeneous dispersion was observed. Then, 75 mL of an $FeCl_2$ (98% Sigma Aldrich) solution in methanol (25×10^{-3} M) were added and the mixture was subjected to reflux at 90 °C for 24 h. After Fe-coordination, the product was filtered, rinsed with MeOH, and washed with 0.5 M H_2SO_4 (95-98% Sigma Aldrich) overnight to remove Fe aggregated species. Finally, the obtained TAP @Fe materials were filtered, rinsed abundantly with distilled water and dried at 80 °C under vacuum.

Site Density, Utilisation and Turnover Frequency

The total Fe site density of the bulk catalyst can be found from the Fe content based on ICP-MS measurement, SD_{ICP} (sites g_{FeNC}^{-1}), according to:

$$\boldsymbol{SD_{ICP} = \frac{(Fe_{ICP}/100) \times N_A}{M_{Fe}}} \qquad \textbf{Eq. 1}$$

Where Fe_{ICP} is Fe wt.% determined by ICP-MS and M_{Fe} is the molar mass of Fe (55.845 g mol^{-1}).

The FeN_x site density of the bulk catalyst based on low-temperature Mössbauer spectroscopy, $SD_{Mössbauer}$ (sites g_{FeNC}^{-1}) can be found from the percentage of doublet species assigned to FeN_x sites, $FeN_{x\,(Mössbauer)}$ (%):

$$\boldsymbol{SD_{Mössbauer} = (FeN_{x(Mössbauer)}/100) \times SD_{ICP}} \qquad \textbf{Eq. 2}$$

In situ nitrite stripping site density was determined using the following equation:

$$\boldsymbol{SD_{Nitrite} = \frac{Q_{strip} \times N_A}{F \times n_{strip}}} \qquad \textbf{Eq. 3}$$

Where $SD_{Nitrite}$ is the site density according to nitrite stripping (sites g_{FeNC}^{-1}), Q_{strip} (C g_{FeNC}^{-1}) is the nitrite reductive stripping charge determined from the stripping peak, n_{strip} is the number of electrons associated with the reduction of one adsorbed nitrosyl per site and its value is assumed as five, N_A is Avogadro's constant (6.023×10^{23} mol^{-1}) and F is Faraday's constant (96,485 C mol^{-1}).

Two utilisation percentages of FeN_x sites can be calculated according to the following:

$$\boldsymbol{Utilisation_{Nitrite/(Mössbauer)} = \frac{SD_{Nitrite}}{SD_{(Mössbauer)}} \times 100(\%)} \qquad \textbf{Eq. 4}$$

$$\boldsymbol{Utilisation_{Nitrite/ICP} = \frac{SD_{Nitrite}}{SD_{ICP}} \times 100(\%)} \qquad \textbf{Eq. 5}$$

Where $Utilisation_{Nitrite/(Mössbauer)}$ is the number of electrochemically accessible FeN_x sites to number of bulk FeN_x sites and $Utilisation_{Nitrite/ICP}$ is the number of electrochemically accessible FeN_x sites to number of bulk Fe atoms.

Electrochemical measurements

Electrochemical oxygen reduction tests were carried out employing an AUTOLAB PGSTAT302N in N_2 (≥99.99998% BIP® Plus, Air Products) and O_2 (≥99.9998% Ultrapure Plus, Air Products) saturated 0.1 M $HclO_4$ (Suprapur®, Merck) electrolyte in a compartment glass cell with a three-electrode configuration using $Ag/AgCl_{sat}$ (3M KCl) as reference electrode and a glassy carbon rod as counter electrode. *iR* correction was applied post electrochemistry by determining the solution ohmic drop R (23 Ω) from the intercept of the imaginary impedance

axis in the Nyquist plot (not fitted with an equivalent circuit) via electrochemical impedance measurement between from 10^{-5} – 10 Hz at open circuit potential. A 5 mm glassy carbon rotating disk electrode (RDE, Metrohm) was polished with a micropolish cloth and 0.05 μm alumina suspension (Buehler). The TAP-derived catalysts were drop-casted on to a freshly polished RDE; 13 μL of an ink comprising 4 mg of the catalyst, 480 μL of 18.2 MΩ cm deionised water, 480 μL of isopropanol (≥99.5% Honeywell™, Fisher Scientific) and 40 μL of 5wt% Nafion® D-521 (5% w/w in water and 1-propanol, Alfa Aesar) which was freshly sonicated for 30 mins in the corner of a bath sonicator (132 kHz ultrasonic cleaner, VWR). The drop-cast ink was dried at 700 rpm for 30 min under ambient air, leading to a catalyst loading of 0.26 mg_{FeNC} cm^{-2}. The reference electrode was calibrated before each electrochemical test in a separate cell in 0.1 M $HclO_4$ purged with hydrogen (1 bar) for 10 min. During the calibration, a 3 mm Pt RDE tip (Metrohm) working electrode was rotated at 1,600 rpm for 5 cyclic voltammograms at 10 mV s^{-1} between -0.26 to -0.28 $V_{Ag/AgCl}$ with a Pt rod (Metrohm) and $Ag/AgCl_{sat}$ as a counter and reference electrode, respectively. An average value for the conversion between $Ag/AgCl_{sat}$ and RHE was obtained from the forward and backward scans at zero current.[33] Cyclic voltammograms were obtained after purging the electrolyte for at least 15 min and recorded at 50 mV s^{-1} at 0 rpm for N_2 saturated (measurements at 10th cycle displayed), and 10 mV s^{-1} at 1,600 rpm when the electrolyte was saturated with O_2 or N_2 (measurements at 3rd cycle displayed). The pseudocapacitance was corrected for by subtracting N_2 saturated measurements at 1,600 rpm from the O_2 saturated results. In the case of the best performing material (observed in the cathodic scans of the cyclic voltammograms under O_2 at 1600 rpm), electrochemical measurements were repeated 5 times. The kinetic current density (j_{kin}) at 0.80 and 0.85 V_{RHE} was determined from the geometric disk current density (j_d) and geometric diffusion-limited current density (j_{lim}) at 0.3 V_{RHE} according to the Koutecký–Levich Equation 1:

$$\boldsymbol{j_{kin} = \frac{j_d \times j_{lim}}{j_{lim} - j_d}} \qquad \textbf{Eq. 6}$$

Subsequently, the kinetic mass activity at 0.80 and 0.85 V_{RHE} can be found:

$$\boldsymbol{m_{kin} = \frac{j_{kin}}{Loading_{FeNC}}} \qquad \textbf{Eq. 7}$$

Where m_{kin} is the kinetic mass activity at 0.80 or 0.85 V_{RHE} (A g_{FeNC}^{-1}) and $Loading_{FeNC}$ is the catalyst loading on the RDE (mg_{FeNC} cm^{-2}).

Electrochemical measurements were carried out in a RRDE to calculate the number of electrons transferred. The ink formulation and loading were identical to those used during RDE measurements. The Pt ring was set to 1.27 V_{RHE}. The number of electrons transferred (n) was calculated from the disk and the ring current using the following equation:[34]

$$\boldsymbol{n = 4 \times \frac{j_d}{j_d + \frac{j_r}{N_c}}} \qquad \textbf{Eq. 8}$$

Where j_r is the ring current and N_c is the measured collection efficiency (21.67%). N_c calibration was obtained according to the protocol of Zhou et al.[34] Briefly, chronoamperometric measurement over 60 s in the same cell configuration as above (0.26 mg_{FeNC} cm^{-2} catalyst, 1,600 rpm) under N_2 saturated conditions, with additional 0.004 M $K_3Fe(CN)_6$ (EMSURE® ACS, Reag. Ph Eur, Sigma Aldrich) and the disk and ring set to 0.1 V and 1.27 V_{RHE},

respectively. The last 10 s of chronoamperometry were averaged to obtain j_r and j_d and N_c calculated via the following equation:

$$N_c = \frac{j_r - j_{r0}}{j_d} \qquad \textbf{Eq. 9}$$

Where j_{r0} includes anodic current not arising from reduced $Fe(CN)_6^{4-}$ on the disk.

Additionally, the H_2O_2% was obtained from Equation 10:

$$H_2O_2\,\% = 2 \times \frac{\frac{j_r}{N_c}}{j_d + \frac{j_r}{N_c}} \times 100 \qquad \textbf{Eq. 10}$$

Accelerated stress test cyclic voltammetry cycles were conducted between 0.8-0.4 V_{RHE} at 100 mV s^{-1} under O_2-saturation, with Pt ring applied at 1.27 V_{RHE} throughout.

In situ nitrite stripping was conducted, based on recently updated protocol,[18] to determine site density and turnover frequency (TOF). 5 mg of FeNC was mixed with 519 µL isopropanol and 519 µL H_2O and 54 µL Nafion® (5wt% solution, Sigma-Aldrich) to prepare the catalyst ink which was then bath sonicated for at least 30 minutes. The catalyst ink was deposited on a 5 mm glassy carbon disk of a rotating disk electrode (Pine Instruments, model AFE6R1AU and rotator model AFMSRCE) by drop casting and dried at room temperature (rotating around 200-300 rpm), ultimately reaching a catalyst loading of 0.2 mg_{FeNC} cm^{-2}. All the electrochemical measurements were performed in a 0.5 M sodium acetate buffer (sodium acetate (99%, Sigma-Aldrich), glacial acetic acid (AnalR Normapur, VWR) and ultrapure water (MilliQ 18.2MΩ cm) as electrolyte (pH 5.2). The catalyst cleaning protocol consisted of measuring two cyclic voltammetry cycles in O_2-saturated electrolyte at 5 mV s^{-1} scan rate between 1.0-0.3 V_{RHE}, followed by 10 cyclic voltammetry cycles in a N_2-saturated electrolyte at 100 mV s^{-1} scan rate between 1.0-0.3 V_{RHE} and 5 cyclic voltammetry cycles at 10 mV s^{-1} scan rate. These steps were repeated twice. O_2-saturated cyclic voltammetry measurements were repeated a third time before progressing with the remainder of the nitrite stripping protocol. A current integrator was used while performing the nitrite stripping cyclic voltammetry scans for an accurate determination of the stripping charge. The catalyst poisoning step, measurement conditions of the O_2 reduction activities and nitrite stripping CVs at the unpoisoned, poisoned and recovered stages were the same as previously reported,[35] with the addition of a second nitrite poisoning on the recovered catalyst. O_2 reduction was not measured in between the unpoisoned, poisoned and recovered stages during the second poisoning measurements. The purpose of the second poisoning was to minimize any potential variation in the baseline CV current due to the involvement of O_2 reduction steps.

TOF values were determined from *in situ* nitrite stripping in the range of 0.80-0.85 V_{RHE} based on the following equation:

$$TOF = \frac{(j_{k(unpoisoned)} - j_{k(poisoned)}) \times N_A}{SD_{Nitrite} \times F} \qquad \textbf{Eq. 11}$$

Where $j_{k(unpoisoned)}$ is the unpoisoned kinetic mass activity and $j_{k(unpoisoned)}$ is the poisoned kinetic mass activity.

Results and discussion

Nitrogen-doped carbon materials were prepared by pyrolysis of 2,4,6-Triaminopyrimidine (TAP) in the presence of $MgCl_2{\cdot}6H_2O$ at temperatures between 800 to 1000°C. TAP has been used previously as C-dopant in polymeric semiconductors and covalent organic materials to improve electronic conductivity and photocatalytic

performance,[36,37] however its use as building block for conductive carbon-based electrocatalysts remains in its infancy,[38] and its polymerization pathway has not been elucidated up to date. In this work we selected TAP due to its structural similarities to melamine (Figure S1); melamine serves as precursor to the polymeric semiconductor graphitic carbon nitride (Figure S2),[39] which has been widely explored as a platform for single and dual atom catalysts.[7,40,41] Nevertheless its wide band gap (2.7 eV) and its decomposition at high temperatures (over 700°C) do not allow the formation of a conductive scaffold and therefore hinder its exploitation in electrochemical devices.[42] TAP can serve as a building block for a conductive N-doped carbon material that provides a suitable coordination environment for metallic ions. We hypothesize that upon thermal condensation, TAP releases NH_3 and forms reaction intermediates analogous to melem (a heptazine-like unit), present in the pyrolysis of melamine and other triazine-based molecules,[43] at higher temperatures (400-500°C) a polymeric material similar to graphitic carbon nitride would be formed and subsequently decompose through the release of C-N based radicals resulting in a N-doped carbon material (**Scheme 1**). Additionally, the utilisation of $MgCl_2{\cdot}6H_2O$ as a porogen allows the self-assembly of TAP *via* N-H···O hydrogen bonds with the water molecules followed by polymerization in an entirely molten state (**Figure 1a**), as TAP displays a melting point at 235 °C (as confirmed by differential scanning calorimetry in Figure S3). The molten intermediate in triazine-based molecules upon pyrolysis has been proven very efficient for the synthesis of carbon-based materials,[44] and in this case provides a homogeneous state for the polymerization and optimal dispersion of the Mg sites, leading to ultrahigh porosity at high temperatures.[45]

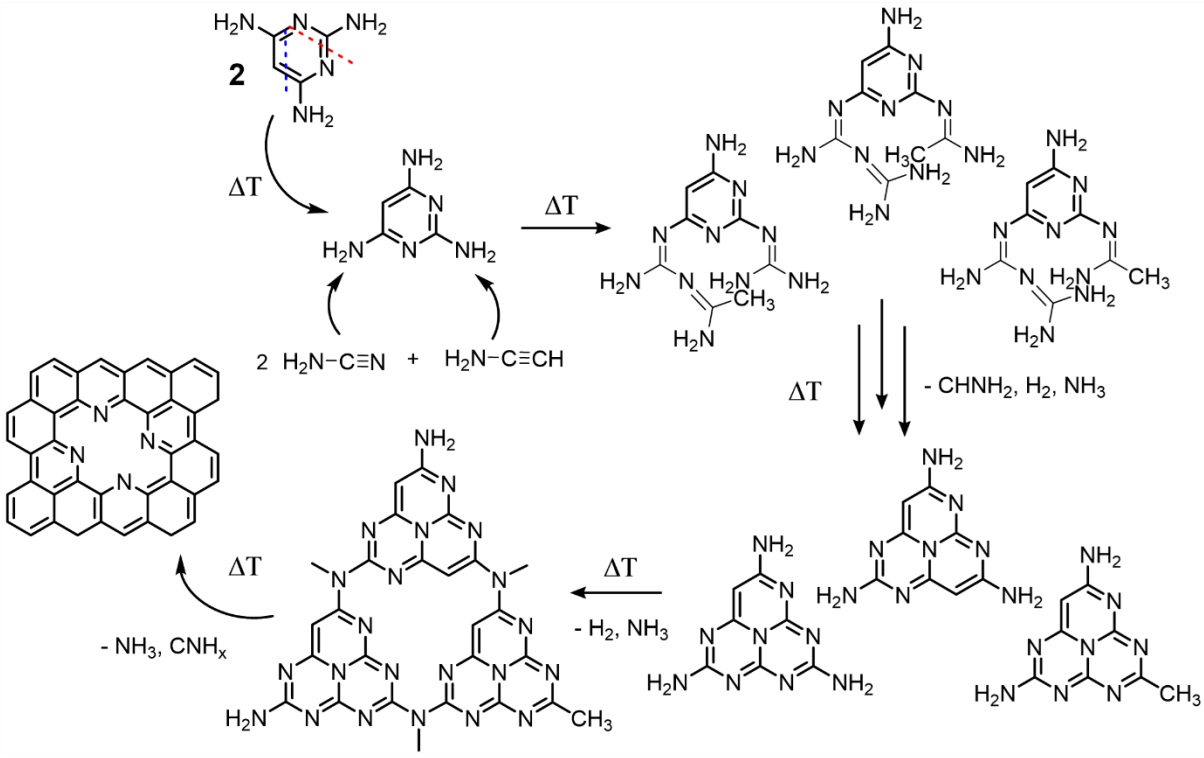

Scheme 1. Suggested polymerization pathway of 2,4,6-Triaminopyrimidine.

We carried out thermogravimetric analysis coupled to mass spectrometry (TGA-MS) to study the conversion of TAP into a conductive carbon framework. TGA curves show a 66% loss in mass between 200 and 320°C mostly due to the release of ammonia ((*m/z*) = 17), along with low molecular weight molecules, including ethynamine (C_2H_3N (*m/z*) = 41) or cyanamide (CN_2H_2, (*m/z*) = 42) amongst others (Figure 1b, Figure S4). The release of

ammonia, cyanamide, and ethynamine suggests the formation of reaction intermediates that lead to a carbon nitride-like polymer similar to that proposed by May (Scheme 1).[46] While melamine can decompose in three cyanamide fragments, TAP decomposes in a mixture of cyanamide and ethynamine, which react with pristine TAP leading to conductive melem-like scaffolds with direct C-C bonds. From 320 to 700°C just a 14% decrease in mass is observed (Figure 1b), with species detected in the mass spectrometer heavier than those detected at lower temperature, mostly cyanide-based (cyanogen $(CN)_2$, (*m/z*) = 52), ammonium cyanide CH_4N_2 (*m/z*) = 44, isocyanoethene C_3H_2N (*m/z*) = 52), etc. This fact suggests the decomposition of the tertiary amine bonds connecting heptazine-like units in the polymeric material by release of radicals, leading to a N-doped carbon material with a 12% yield at 800°C.[47]

TAP was pyrolyzed under N_2 atmosphere at 300, 500 and 700°C (Figure S5) to study the properties of the different reaction intermediates. X-ray diffraction (XRD) patterns show a highly ordered crystalline structure for the initial TAP building block (Figure S6). Such crystallinity decreases as pyrolysis temperature increases as evidenced by the broadening of the diffraction peaks; and at 500 °C a peak at 2Θ = 13.2° emerges suggesting certain degree of in plane order like that observed in polymeric carbon nitrides.[48] Additionally, the (002) stacking peak of graphitic structures can be observed at 2Θ = 26.8° at 500 and 700°C. XPS measurements were conducted in each of the samples to evaluate the change in chemical and electronic states of C and N upon thermal treatment. C1s spectra of TAP shows 3 different binding energies corresponding to structural and adventitious C-C at 284.7 eV, C-$(N)_3$ at 285.7 eV, and C-$(N)_2$ at 287.9 eV (Figure 1c); and N1s resembles just two contributions that belong to N embedded within the pyrimidinic ring (399.3 eV) and amine groups (400 eV, Figure 1d). After pyrolysis at 300°C, the chemical states in both C1s and N1s are very similar to that of the molecular building block and just a slight increase in the C/N ratio can be observed (Table S1) owing to the initial release of ammonia (as confirmed by TG-MS) and formation of a molecular melem analogue (Scheme 1). However, the C1s spectra of TAP 500°C shows a much higher at.% of the C-$(N)_3$ contribution (located at 286 eV), suggesting the formation of tertiary amine linkages between monomeric melem-like units. A new contribution appears at high binding energies (288.3 eV) probably owing to the partial degradation of the C-N lattice and formation of cyanamide moieties as suggested by the TGA-MS data.[49] In the N1s spectra the wt.% of the contribution that belongs to amine groups substantially decreases from 67 and 52% in TAP and TAP 300, respectively, to 38% in TAP 500 (Table S2) as well as the overall nitrogen content (55 and 46% in TAP and TAP 300, respectively, to 38% in TAP 500), further supporting the formation of a polymeric network by release of nitrogen moieties. Finally, TAP 700 displays the common features of a N-doped carbon material; C1s spectra shows the presence of three contributions corresponding to C-C, C-N and C≡N/C=O bonds with an overall C/N ratio of 2, similar to that of C_2N covalent organic materials.[50] ^{13}C Solid-state NMR was employed to further elucidate the evolution of TAP into a conductive C-N framework upon pyrolysis (Figure S7). Bare TAP shows three different chemical shifts at 164, 162 and 75 ppm, which correspond to C-C-$(N)_2$, C-$(N)_3$ and C=C sp2 within the ring, respectively.[51] Upon pyrolysis the C-$(N)_3$ contribution broadens to 157 ppm, indicating the appearance of CN_3 species due to the TAP trimerization (Scheme S1) similar to the one observed by Schnick and co-workers in melem, additionally the C=C sp2 shifts to 80 ppm.[43,52] At 700°C the material becomes more conductive, and the N=C-NH_2 peak (165 ppm) disappears in favour of graphitic carbons (100-150 ppm) and CN_3 (151 ppm).

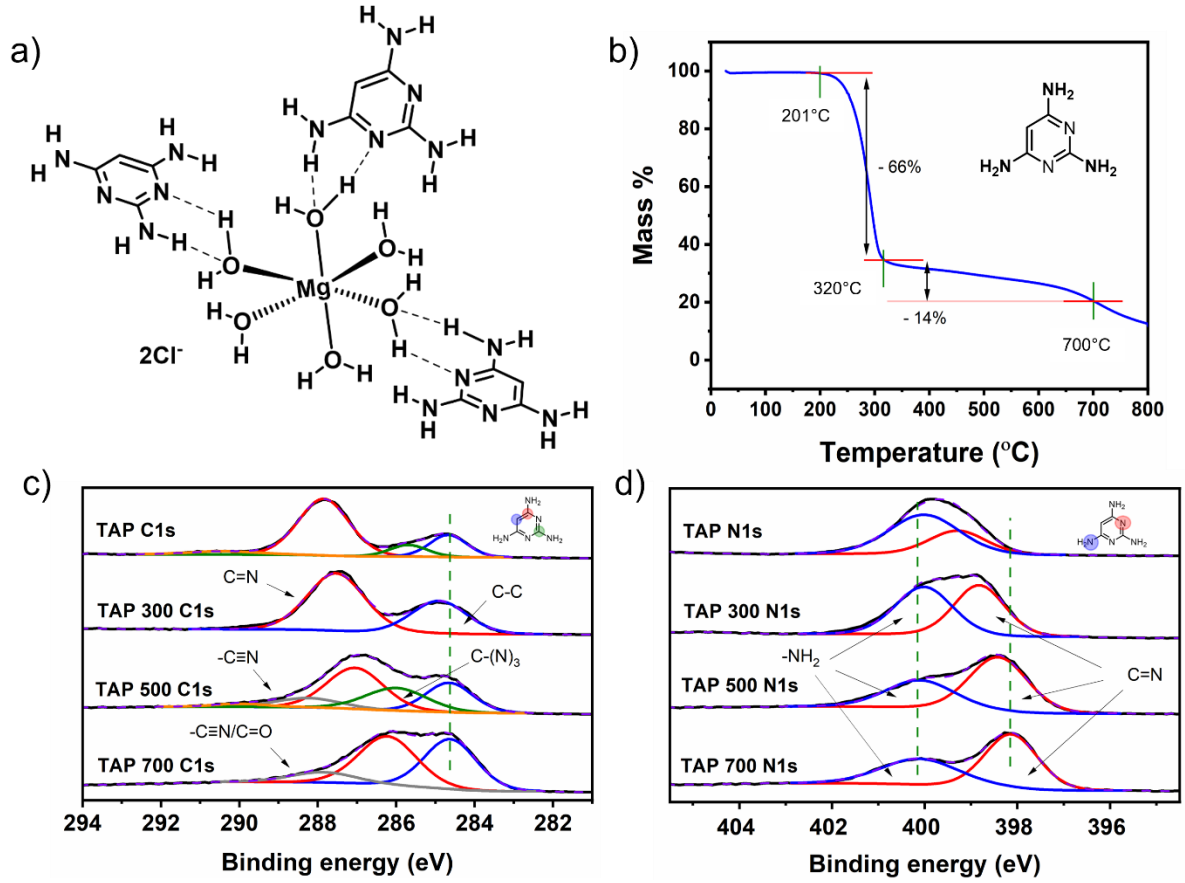

Figure 1. Representation of the self-assembly between 2,4,6-Triaminopyrimidine and $MgCl_2{\cdot}6H_2O$ (a). TGA curve of TAP (b). C1s (c) and N1s (d) XPS spectra of TAP pyrolyzed at 300, 500, and 700 °C.

While the features of such materials are suitable for the coordination of metallic atomic species, the high nitrogen content hinders the electronic conductivity, which is sought after in electrochemical applications, as well as a high porosity. Therefore, after elucidating the growth mechanism of TAP into a conductive C-N framework, we pyrolyzed it in the presence of $MgCl_2.6H_2O$ at higher temperatures (800-1000°C) to achieve suitable nitrogen content, conductivity, and porosity. TGA-MS shows a very similar polymerization pathway in the presence of $MgCl_2$ (Figure S8-9). The TGA curve shows a stepwise mass loss below 250°C, associated with the step-by-step elimination of crystal water from $MgCl_2{\cdot}6H_2O$, to yield $MgCl_2{\cdot}4H_2O$ (65°C-120°C), $MgCl_2{\cdot}2H_2O$ (120°C-160°C), $MgCl_2{\cdot}H_2O$ (160°C-195°C), $MgCl_2$ (195°C-245°C, Figure S8). The mass spectrometry data clearly shows the corresponding release of water ((*m/z*) = 18) for each step, with the additional release of HCl ((*m/z*) = 36) at the last dehydration step and again above 450°C, indicating the conversion of $MgCl_2$ to MgOHCl as suggested in previous reports.[45] The onset of TAP decomposition is higher than in the absence of $MgCl_2{\cdot}6H_2O$ and TAP decomposition products are observed in a quite narrow temperature window of 350°C to 400°C. In the presence of magnesium, we observe the same decomposition product as for the pure TAP, including ammonia, amine-based molecules, and low molecular weights cyanides. This suggest that the presence of $MgCl_2{\cdot}6H_2O$ does not alter the polymerization pathway of TAP.

After pyrolysis at 800-1000 ˚C, the materials show a highly amorphous structure owing to the enhanced surface area compared to the pyrolysis in the absence of porogen (Figure S10), and just a weak diffraction peak at 2Θ = 26.4° can be observed in TAP 800 corresponding to the (002) interlayer stacking peak. From N_2 sorption

measurements, the specific surface area reaches up to 3,293 m^2 g^{-1} for TAP 900, according to Brunauer-Emmett-Teller (BET) analysis (**Figure 2**a, Figure S11), being micro- and mesoporous in nature as shown previously in similar materials prepared through ionothermal methods,[45,53]. In all pyrolysed TAP materials a bimodal pore size distribution is observed. The smallest pore size is centred around 0.7-1 1 nm, indicating the presence of suitable micropores for the coordination of metal-based moieties (Figure 2b). Large micropores to small mesopores (1-4 nm) are also present, along with a small portion of large mesopores around 40 nm, adding to the available pore volume (Figure 2b). The total micropore volume steadily decreases from TAP 800 (0.91 cm^3 g^{-1}) through to TAP 1000 (0.58 cm^3 g^{-1}), possibly due to collapse of micropores with increasing temperature. Meanwhile, total mesopore volumes markedly increase from 0.90 cm^3 g^{-1} to 1.95 cm^3 g^{-1} when pyrolysis of TAP increases from 800 ˚C to 900 ˚C (Figure S12), suggesting a high availability of nitrogen sites for Fe coordination and subsequent reactant and product accessibility after pyrolysis at temperatures of 900 ˚C or greater. Remarkably, TEM images of TAP 900 further confirm the formation of a high surface area amorphous material (Figure S13). Raman spectroscopy shows a lower D/G band intensity ratio (I_D/I_G) at higher pyrolysis temperature, suggesting a higher degree of dopants and defects in TAP 800, and the formation of a defective graphene-like material with low nitrogen content and higher graphitization degree at 1000 ˚C (Figure S14).

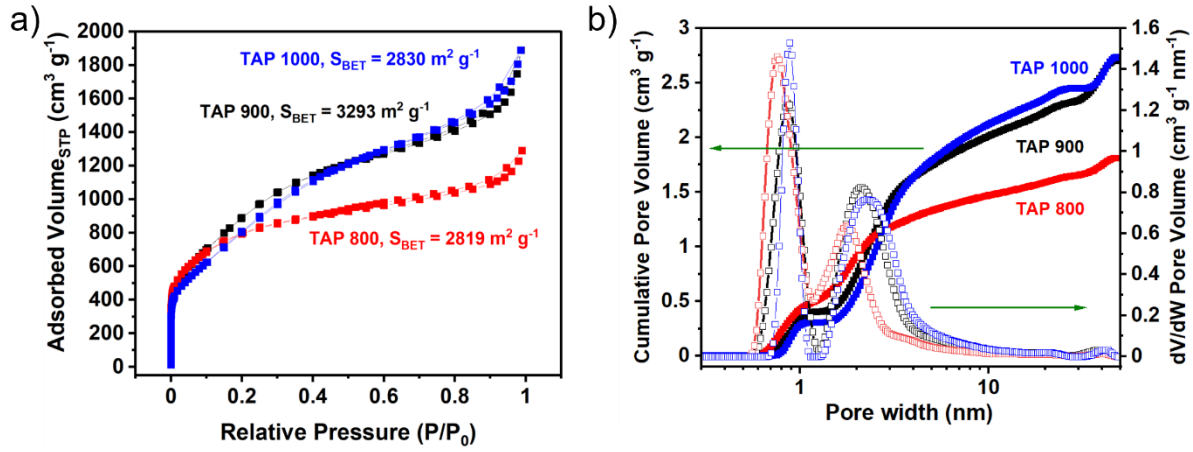

Figure 2. N_2 sorption isotherms with specific BET surface areas labelled (a) and corresponding pore size distributions and cumulative pore volumes calculated using 2D-NLDFT heterogeneous surface carbon model in SAIEUS software (b) of TAP-derived materials.

The decrease in nitrogen content upon pyrolysis at higher temperatures was corroborated by XPS measurements (Figure 3b, Table S4); while TAP 800 shows 23.5 at.% (probably hindering its electrical conductivity), TAP 900 and 1000 display 4.5 and 1.8 at.%, respectively. Such values represent a suitable content of heteroatoms with lone electron pairs that can coordinate with Fe species leading to single atom catalysts without suppressing the conductivity of the material.[39] Both C1s and N1s spectra of the TAP derived materials shows very similar profiles; C1s displays chemical binding energies that stand for C-C, C-N and C=O bonds (Figure S15), while the N1s presents three main contributions that stand for pyridinic, pyrrolic and graphitic nitrogen. Interestingly, in TAP 900 a new contribution emerges suggesting coordination with remaining Mg species (the permanency of small quantities of Mg has been confirmed by ICP-MS, Figure S16). While certain Mg may be coordinated as well in TAP 800, the low N content and signal to noise ratio in TAP 900 allows the visualization of minority N

chemical states. Additionally, at 1000°C, the band corresponding to pyrrolic N (at 401.2 eV) becomes dominant indicating either the degradation of pyridine-like moieties or their conversion in pyrrolic motifs.[54]

Fe coordination in TAP 800-1000, was carried out through low temperature methanol reflux with a $FeCl_2$ salt (**Figure 3**a).[19] XPS and ICP-MS confirm the successful introduction of Fe within TAP 900@Fe, with values of 0.70 and 0.52 wt.% Fe, respectively. According to ICP-MS, TAP 900 contained 0.39 wt.% Mg and 0.18 wt.% Fe (Fe likely derived from contaminants in the TAP precursor), while only 0.02 wt.% Mg remained in TAP 900@Fe (Figure S16). The 0.34 wt.% (0.073 at.%) increase in Fe and 0.37 wt.% (0.183 at.%) decrease in Mg from TAP 900 to TAP 900@Fe suggests the low temperature Fe coordination enables the transmetalation of Mg for Fe. Similar observations are seen for TAP 1000 to TAP 1000@Fe, although not for TAP 800 to TAP 800@Fe (Figure S16). We focus subsequent in-depth characterization on TAP 900@Fe owing to its higher electrocatalytic activity as shown below. In TAP 900@Fe N1s XPS spectra, a peak arises at 399.5 5 eV that can be assigned to N-Fe coordination, accounting for 34.5 at.% (Figure S17). Compared to TAP 900, the total contribution of pyridinic moieties decreases from 29.2% to 16.9% and the one corresponding to nitrogen coordinated to metals (Mg in the case of TAP 900 and Fe in the case of TAP 900@Fe) increased from 18% to 34.5%, while the pyrrolic components remain similar (Figure 3c, Table S5). This fact suggests that Fe is coordinated via pyridinic N rather than pyrrolic. Additionally, XRD patterns suggest the absence of large, aggregated Fe-based particles, as no diffraction peaks corresponding to Fe oxides, carbides or metallic Fe can be observed (Figure S18).

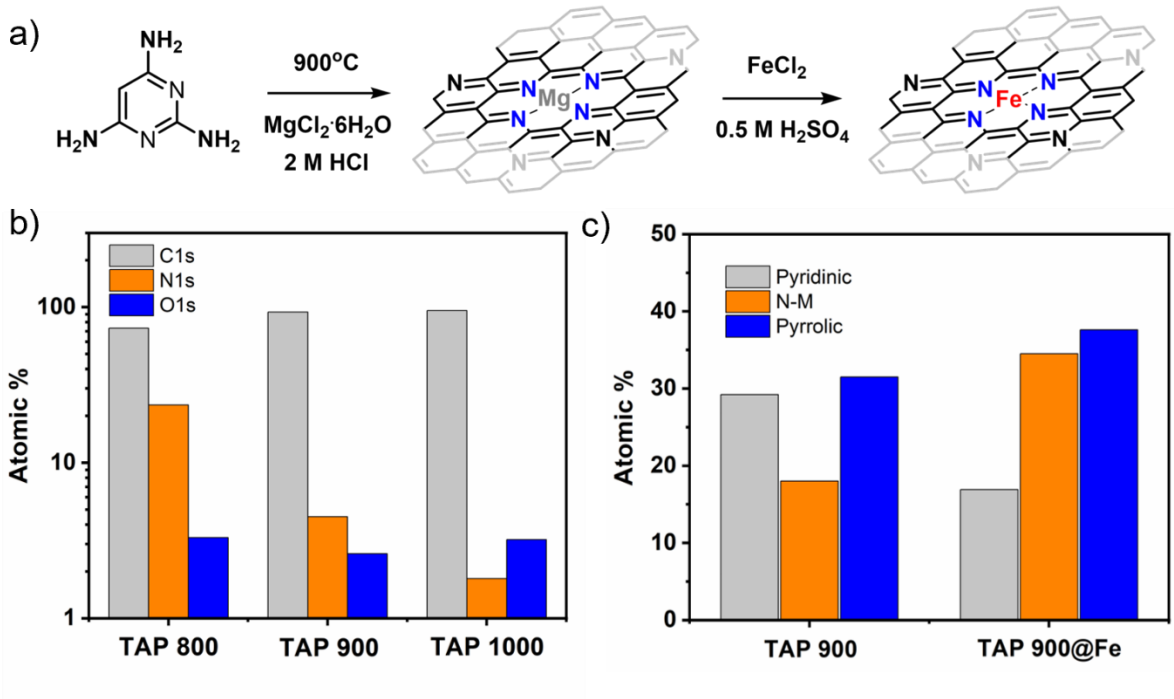

Figure 3. Schematic representation of Fe coordination in TAP-derived materials (a). Elemental composition of TAP-derived materials obtained by XPS plotted in a logarithmic scale (b) and deconvolution of XPS N1s species in TAP 900 and TAP 900@Fe (c).

The nature of the Fe within TAP 900@Fe was further studied through high angle annular dark field scanning transmission electron microscopy (HAADF-STEM). HAADF-STEM images show bright dots embedded in an

amorphous matrix corresponding to isolated Fe sites within N-doped Carbon (**Figure 4**a-c) and the absence of aggregated Fe species (Figure S19). Furthermore, both C, N, and Fe are homogeneously distributed through the material as shown by atomic resolution elemental mapping in energy dispersive x-ray spectroscopy (EDX) (Figure 4d-f); oxygen can be also found arising from surface functionalities (Figure S20), as observed previously through XPS data (Table S4).

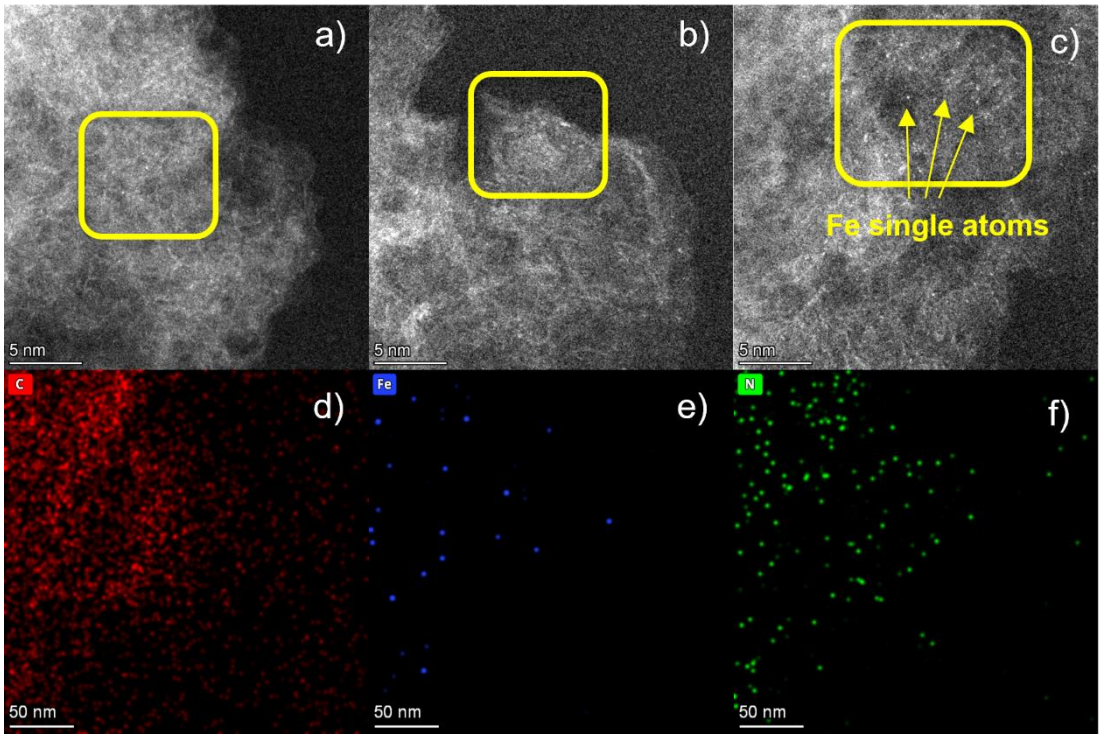

Figure 4. HAADF-STEM images showing distributed single atoms (a-c) and atomic resolution EDX profile elemental maps for C (d), Fe (e), and N (f) of TAP 900@Fe.

Using *ex situ* X-ray absorption spectroscopy, the oxidation state and coordination environment around TAP 900@Fe were further assessed. **Figure 5**a shows the comparison of Fe-*K* edge XANES spectra of TAP 900@Fe with respect to the reference samples- Fe foil, Fe_2O_3, $Fe^{II}Pc$ and Cl-$Fe^{III}Pc$. TAP 900@Fe absorption edge is the highest and marginally higher than Fe_2O_3, suggesting the +3 oxidation state of Fe. Distinct changes are observed even in the pre-edge range. The signature peak of 7118 eV in $Fe^{II}Pc$ can be attributed to the FeN_4 moiety, which has a preserved D_{4h} symmetry around Fe and arises due to 1s → $4p_z$ electronic transition. However, TAP 900@Fe shows a peak at 7113 eV instead of 7118 eV, indicating a distorted square planar geometry, which is probably due to an axial coordination of -N/-O or Cl^- arising from the Mg^{2+} templating agent. Fourier transformed EXAFS comparison in Figure 5b indicates the absence of Fe-Fe peak and the formation of single Fe atoms within the TAP 900@Fe catalyst, which corroborates the HAADF-STEM results. *Ex situ* cryo (5 K) EPR was used to study the unpaired electrons within TAP 900 and TAP900@Fe (Figure 5c). The small sharp g ~2 signal in TAP 900@Fe arises from background signals from the resonator and empty EPR tube. Meanwhile, the large and sharp g ~2 signal in TAP 900 is likely from organic radicals from defects in the carbon matrix which seem to be removed during the subsequent metalation or acid washing process. Interestingly, the signal of TAP 900@Fe closely resembles EPR results from a Fe-doped $CaBi_2Nb_2O_9$ material.[55] The g ~ 4.3 value is assigned to high spin Fe^{3+} with rhombic zero field splitting (E/D = 1/3),[9,55] while the weak shoulder at g ~ 9.6 has been previously assigned

to Fe^{3+} with lower rhombicity $E/D \leq 1/3$.[55] Finally, a broad axial signal between $g = 6$ and $g = 2$ is also observed in TAP 900@Fe, previously characterised as high spin Fe^{III} with large axial zero field splitting owing to a square pyramidal or quasi octahedral coordination environment.[9,56]

Low temperature Mössbauer spectra with an external low (60 mT) and high (7 T) magnetic field were recorded to help resolve the Fe sites, with best fit simulations yielding five separate Fe assignments (Figure 5d, Table S6). It should be noted that low-field spectrum revealed a small amount (≤10%) of slow-relaxing paramagnets that are assigned to ferric oxide aggregates; since no oxide phases were present in the XRD, we assume that that these aggregates display sizes of <2nm.[57] They are visible as a distortion of the baseline, but their proportion was too low for any features to emerge from the noise. We neglected these oxide phases on both spectra, allowing the baseline allowed to move down. A distinct Fe^{III} high spin (HS) component D1 (41%) is identified with fit E/D = 0, which correlates with the broad axial signal in EPR ($g = 2$ and $g = 6$). Minority species D2 (17%), D3 (13%), D4 (18%) and D5 (11%) are also found and are further discussed in Supplementary Note 1. We focus the discussion on the signal corresponding to D1, owing to its dominance and its suggested higher activity.[10] The isomer shift (δ = 0.47 mm s^{-1}) and quadrupole splitting (ΔE_Q = 1.05 mm s^{-1}**)** of component D1 matches closely with a penta-coordinated FeN_4 with a N axial ligand (resembling a heme moiety) identified by Wagner *et al.* through nuclear inelastic scattering and EPR.[12] Meanwhile, a similar D1 component has been assigned to a penta-coordinated $Fe^{III}N_4C_{12}$ with axial O ligand based on DFT calculations and Mössbauer spectroscopy.[10,58]

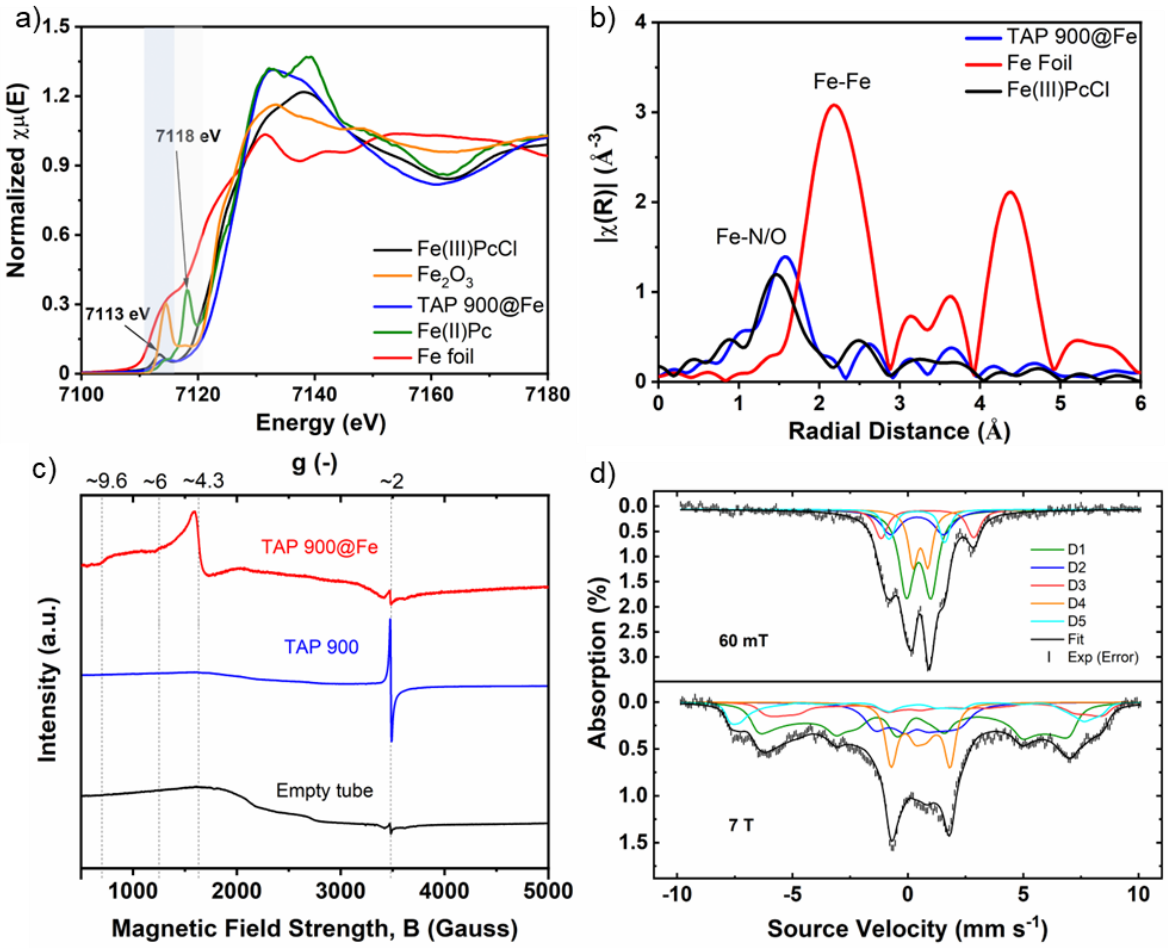

Figure 5. Fe *K*-edge XANES spectra of as prepared TAP 900@Fe in comparison with Fe foil, Fe_2O_3, $Fe^{II}Pc$ and $Fe^{III}PcCl$ showing that average Fe in the synthesized sample is in +3 oxidation state (a). Fourier Transform of TAP 900@Fe, Fe foil and $Fe^{III}PcCl$ indicating the absence of Fe-Fe bond in TAP 900@Fe (b). Cryo (5 K) X-band EPR signals of TAP 900, TAP 900@Fe and empty quartz EPR tube (c). Low-temperature Mössbauer spectrum of TAP 900@^{57}Fe recorded at T = 5.3 K in a weak (60 mT) or a strong magnetic field (7 T) applied parallel to the gamma rays (d). The five Fe components are assigned to Fe^{III} HS (D1 - green), Fe^{II} IS (D2 – blue), Fe^{II} HS (D3 - red), Fe^{II} LS (D4 - orange) and Fe^{III} HS (D5 - turquoise). Solid black line indicates the compound spectrum and vertical black lines indicate error bars of measured spectrum.

To investigate the electrochemical O_2 reduction activity of the prepared materials we employed them in a three-electrode system with O_2-saturated 0.1 M $HClO_4$ as electrolyte. The metal-free counterparts were inactive for O_2 reduction (**Figure 6**a, Figure S21), and after Fe addition TAP 900@Fe showed the highest catalytic activity, with kinetic current density, J_{kin} (Eq. 6), = -1.04 ± 0.12 mA cm^{-2} at 0.8 V_{RHE} and a corresponding kinetic mass activity, m_{kin} (Eq. 7), of 4.0 ± 0.46 A g_{FeNC}^{-1}. TAP 800@Fe remained nearly inactive, possibly due to the high nitrogen content limiting its conductivity. Meanwhile TAP 1000@Fe showed only slightly lower mass activity than TAP 900@Fe, reaching J_{kin} = -0.76 mA cm^{-2} at 0.8 V_{RHE} and corresponding mass activity of 2.9 A g_{FeNC}^{-1}. Comparison of optimally performing TAP 900@Fe kinetic mass activity to other high performing FeNC O_2 reduction electrocatalysts reported in the literature is shown in Figure S22. The selectivity towards the 2-electron H_2O_2 formation was initially negligible over the potential range (<3%, Eq. 8-10, Figure 6b, Figure S23a,b). RRDE accelerated stress testing was applied under O_2-saturation in a narrow cyclic voltammetry potential window of 0.4-0.8 V_{RHE} at 100 mV s^{-1} to focus on the carbon oxidation effect of local H_2O_2 production[59] and Fe demetalation on TAP 900@Fe performance, while avoiding direct carbon oxidation at high potentials (>1.0-1.1 V_{RHE} at room temperature) on FeN_x sites.[60] The Pt ring was held at 1.27 V_{RHE} during the accelerated stress test to reduce build-up of H_2O_2 in the electrolyte. Even after 8,000 cycles, TAP 900@Fe remained selective to the 4e$^-$ process, with H_2O_2 production increasing slightly but remaining <10% between 0.2-0.75 V_{RHE} (Figure 6b, Figure S23a, b). During O_2-saturated accelerated stress test conditions, TAP 900@Fe drops 15% in kinetic mass activity at 0.8 V_{RHE} after 1,500 cycles (3.40 A g_{FeNC}^{-1}). The low H_2O_2 production even after 1,500 cycles may explain the high relative stability of TAP900@Fe, although initial kinetic mass activity is reduced by 46% after 8,000 cycles (2.15 A g_{FeNC}^{-1} Figure S24), potentially due to continued carbon oxidation by local H_2O_2.[59] The atomic Fe sites were assessed by HAADF-STEM post-electrochemistry after 8,000 accelerated stress testing cycles, where Fe single atoms remain within the material, no aggregation occurs, and N and Fe are still homogeneously distributed according to elemental mapping EDX (Figure S25, S26). The possible effect of Fe dissolution in TAP 900@Fe is currently being explored by *in situ* flow cell ICP-MS and will be the subject of upcoming work.

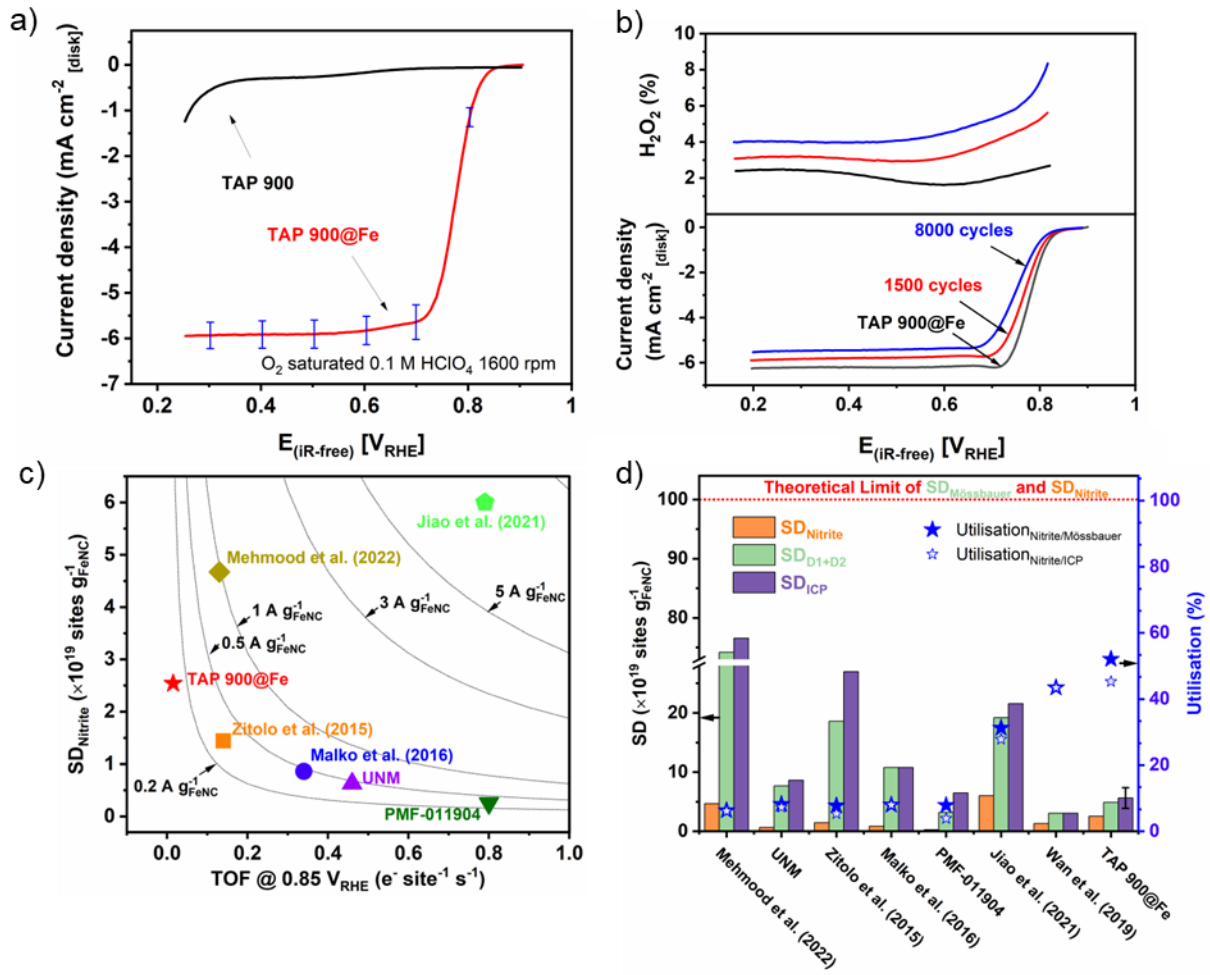

Figure 6. Capacitance-corrected cathodic scan of the cyclic voltammogram in 0.1 M $HClO_4$ (Suprapur) with a rotation rate of 1600 rpm recorded at 10 mV s^{-1} obtained by subtracting N_2-saturated cyclic voltammetry at 1600 rpm from the O_2-saturated result. All measurements were conducted with *iR* correction (23 Ω), 0.26 mg_{FeNC} cm^{-2} catalyst loading and room temperature electrolyte. For TAP 900@Fe, five independent measurements were carried out with the average value plotted and error bars correspond to the standard deviation at the given potential (a). H_2O_2 % production and O_2 reduction current density from cathodic scan RRDE measurements for fresh TAP 900@Fe and after 1500 and 8,000 accelerated stress test cyclic voltammetry cycles (0.8-0.4 V_{RHE} at 100 mV s^{-1} under O_2-saturation with Pt ring applied at 1.27 V_{RHE} throughout). RRDE measured under the same conditions as above with 1.27 V_{RHE} applied to the ring and the Pt ring H_2O_2 oxidation collection efficiency calibrated at the catalyst loading of 0.26 mg_{FeNC} cm^{-2} (b). Comparison of $SD_{nitrite}$ and TOF with corresponding mass isoactivity at 0.85 V_{RHE} (c) of benchmark single atom FeNC catalysts of; Zitolo *et al.* (zeolitic imidazolate framework-8 (ZIF-8) derived),[61] Malko *et al.* (polymerized di-amino naphthalene based),[62] University New Mexico and Pajarito Powder Inc. commercial catalyst PMF-011904 (both silica-templating-based),[28] Mehmood *et al.* (ZIF-8 derived),[18] and Jiao *et al.* (ZIF-8 derived).[17] Part of data obtained is replotted from ref.[63] All $SD_{Nitrite}$ electrochemical measurements with assumed 5 e^- nitrite stripping process in 0.5 M sodium acetate buffer (pH 5.2) in a rotating disk electrode with 0.2 mg_{FeNC} cm^{-2} loading except Wan *et al.* who used 0.27 mg_{FeNC} cm^{-2} and did not present data at 0.85 V_{RHE} (see Fig S28e for 0.80 V_{RHE} data). Different SD and Utilisation metrics for FeNC

catalysts, with the theoretical active SD limit represented by the red dashed line, as calculated by Mehmood *et al.* [18] (d).

The active site density for TAP 900@Fe was assessed through an *in situ* nitrite stripping protocol (Figure S28a-d), assuming a complete five electron reduction of NO to NH_4^+.[35] This gives a lower bound active site density compared to CO cryo-chemisorption, which can probe electrochemically inaccessible sites and can also derive another utilisation factor.[28,64] A high initial $SD_{nitrite}$ of 2.54×10^{19} sites g_{FeNC}^{-1} is observed for TAP 900@Fe (Figure 6c). Kumar *et al*. recently found *in situ* nitrite stripping also probes iron oxides that formed *in situ* as a result of degradation of FeN_x sites.[65,66] No Fe oxides (or other phases) were detected in TAP900@Fe pre- and post-electrochemical testing from HAADF-STEM and elemental mapping EDX (Figure S25, S26), while pre-electrochemical testing low-temperature Mössbauer measurements suggested Fe oxides could exist in a small minority of ≤10% (Figure 5d). The $SD_{nitrite}$ is greater than that of previous benchmark FeNC catalysts,[28] although recent progress with zeolitic imidazolate framework-8 derived catalysts have achieved remarkable $SD_{Nitrite}$ values of 4.7 and 6.0×10^{19} sites g_{FeNC}^{-1}.[17,18] However, these high $SD_{Nitrite}$ FeNC catalysts are still not utilising the vast majority of the loaded FeN_x (<40%, Figure 6d), even in the thin films (~5µm) used in rotating disc electrodes setups during *in situ* nitrite stripping. This raises the question of electrochemical FeN_x utilisation in fuel cells where thick FeNC layers typically around 100 µm are used and uniform ionomer distribution is difficult to achieve. It should be highlighted that some reports claim remarkably high $SD_{Nitrite}$ of 26.3 and 34.7×10^{19} sites g_{FeNC}^{-1}, although with lower SD_{ICP} values of 15.0 and 10.1×10^{19} sites g_{FeNC}^{-1}, respectively.[67,68] These results represent >100% Fe site utilisation, suggesting artifacts in either nitrite or ICP measurements. The $Utilisation_{Nitrite/ICP}$ and $Utilisation_{Nitrite/Mössbauer}$ of TAP 900@Fe is remarkably high at 45% and 52%, respectively (Figure 6d), surpassing the previous record by Wan et al.[27] of 43% achieved at *ca*. half the $SD_{Nitrite}$ and SD_{ICP} (1.33 and 3.05×10^{19} sites g_{FeNC}^{-1}, respectively). It has recently been proposed that nitrite stripping results in NH_2OH product with a total 3 e^- pathway,[69] implying that the $SD_{nitrite}$ would be higher by a factor of 5/3 than the previously elucidated 5 e^- pathway.[70] We would like to note that, if a 3e^- pathway is assumed, the $Utilisation_{Nitrite/ICP}$ and $Utilisation_{Nitrite/Mössbauer}$ of TAP 900@Fe would be 75% and 87%, respectively. The high FeN_x utilisation is attributed to the high mesoporosity (Figure 2, Figure S27), since *in situ* nitrite stripping has been proposed to mainly reach sites in mesopores, and at micropore entries, although not those sites deep within micropores.[28] The mesoporosity in TAP 900@Fe is enabled by a favourable interaction between TAP and Mg^{2+} salt during pyrolysis. Namely, TAP self assembles around the water molecules in the Mg^{2+} salt by hydrogen bonding and upon thermal condensation both components melt (Figure S3) leading to a polymerization in a fully homogeneous liquid-state without grain boundaries and therefore a sufficiently high porosity after acid washing.

Comparing FeNC to Pt/C (Figure S28f), it becomes evident that even if large progress is made to reach 100% FeN_x utilisation, the theoretical accessible SD limit of FeN_x is below that of Pt sites in Pt/C. Therefore, considering only SD, FeNC activity would be insufficient to compete with Pt/C. Hence, FeN_x TOF needs to be considered. While TAP 900@Fe shows an unprecedented FeN_x utilisation, relatively low TOF values of 0.087 and 0.015 e^- $site^{-1}$ s^{-1} at 0.80 and 0.85 V_{RHE}, respectively, were obtained (Eq. 11, Figure 6c, S28e). Low-temperature Mössbauer (Figure 5d) shows D1 Fe^{III} HS is the dominant component in the catalyst. As mentioned earlier, a similar D1 component has been assigned to penta-coordinated $Fe^{III}N_4C_{12}$ with axial O ligand, although this species exhibits

a high TOF.[10] For instance, Jiao *et al.* found their catalyst, which was vastly dominated by $Fe^{III}N_4C_{12}$ with axial O ligand sites (D1 = 90%), exhibited state-of-the-art activity with TOF = 0.8 e^- $sites^{-1}$ s^{-1} at 0.8 V_{RHE}. Meanwhile, a catalyst containing D1 (28%) penta-coordinated $Fe^{III}N_4$ with N axial ligand (TOF not measurable at 0.8 V_{RHE}) displays more comparable activity to that observed with TAP 900@Fe.[12] A N ligand may lead to an undesirable shift in the Fe binding energy and therefore observed lowered TOF. As observed here, the *ex situ* specific active site coordination environment is challenging to elucidate in these materials. FeNC catalysts, even those with purely FeN_x sites, typically contain a range of different active sites. Therefore, to help understand from a fundamental perspective the influence of different axial ligands on the electrocatalytic activity, we investigated axial ligands using DFT simulations of the *OH intermediate in the O_2 reduction reaction volcano (**Figure 7**). While TAP 900@Fe shows a majority of pyridine moieties (Figure 3c), we decided to employ both model pyridine and pyrrole motifs in our DFT calculations (Figure S29, 7b), owing to the varied activity of the two sites.

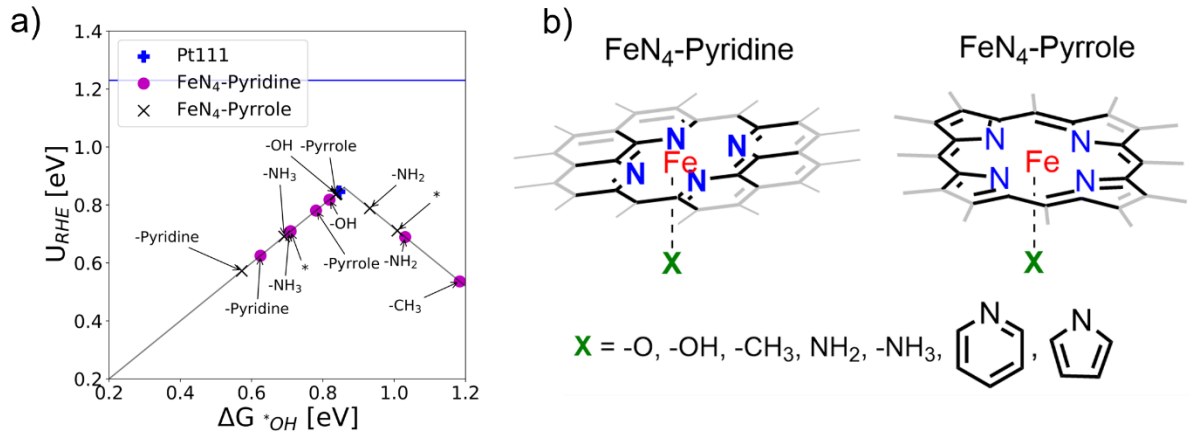

Figure 7. ORR activity volcano represented by O_2 reduction potential (RHE), U_{RHE}, based on *OH binding energies (ΔG_{*OH}) simulated on a series of FeN_4 pyridine and pyrrole sites with different axial ligands, and compared with Pt(111) (a). Schemes showing axial coordination in FeN_4-Pridine (left) and FeN_4-Pyrrole (right), where X denotes the axial ligand (b). -* denotes a pristine FeN_4 structure.

We tested different axial ligands, namely -Pyrrole, -Pyridine, $-NH_3$, $-NH_2$, $-CH_3$, -OH, -O and the pristine structure noted by -*, with simulations of *OH binding energy and compared this with Pt(111) (Figure 7a-b). These different ligands should be thought of as testing how the *OH binding energy on the Fe site changes by having e.g. a nitrogen axial bond represented by $–NH_2$, an oxygen axial bond represented by –OH and etc. Note, as there is no widespread consensus in the literature on modelling MNC systems,[71,72] no water solvation is applied to the *OH binding energies on the FeN_4 sites, while for Pt(111) we use -0.3 eV.[73] In Figure S30, the ORR volcano is shown with -0.3 eV solvation stabilization applied to all binding energies. This points to the fact that the DFT axial trend study is robust on the order of the *OH binding, but the points may shift up and down the volcano depending on the absolute water solvation, which is unknown in MNC systems. Interesting to note in Figure 7a is the pyridine FeN_4 site obtains a weakening of the *OH binding energy via an axial -OH ligand and $-NH_2$ ligand. The axial -OH moves pyridine close to the top of the volcano, while $-NH_2$ deactivates the pyridine FeN_4. Pyrrolic FeN_4 sites, however, display a different trend, the -OH and $-NH_2$ ligands strengthens the *OH binding, placing pyrrole FeN_4 with $-NH_2$ close to the top of the volcano. Very recently, it has been suggested that pyrrolic Fe sites

show a low catalytic activity;[74] our DFT study therefore suggests that their activity could be increased through axial ligand coordination, such as pyrrole or -NH_2. DFT reveals here for the first time that the type, or lack, of axial ligand has a large impact on *OH binding energy for both pyrrolic and pyridinic sites. Our findings imply that the discussion of pyridinic versus pyrrolic sites should consider the important influence of axial ligands.

Conclusions

In summary, we have prepared a highly porous FeNC material with remarkable Fe utilisation for the O_2 reaction in acidic media. The material was prepared in a two-step fashion by Fe coordination in a porous nitrogen-doped carbon material, synthesized employing 2,4,6-Triaminopyrimidine as C-N building block and $MgCl_2{\cdot}6H_2O$ as templating agent for the active site and porosity. The high mesoporosity of the substrate allows the formation of high electrochemically available FeN_x sites. This is confirmed by the record electrochemical FeN_x utilisation of 52% for a high electrochemical active site density of 2.54×10^{19} sites g_{FeNC}^{-1}, as determined by *in situ* nitrite stripping. The most abundant active site is found to be a penta-coordinated FeN_x with axial ligand, as shown by *ex situ* XAS and low temperature Mössbauer spectroscopy. Consequently, DFT revealed the effect of axial ligands on pyridinic and pyrrolic FeN_4 sites, which shows axial ligands can have favourable or unfavourable changes in binding energy of the OH intermediate. We hypothesise that the thorough analysis of the material growth, the record high Fe utilisation and the influence of axial ligands in the O_2 reduction performance of pyridinic and pyrrolic FeN_4 catalysts described here will open new avenues for high-performance single atoms in covalent-organic materials with other reactions such as CO_2 or nitrate reduction. In future studies, such templated, highly porous N-doped carbon supports will be combined with novel metal-coordination techniques (such as ionothermal mixtures and chemical vapor deposition) that allow for a higher metal loading and density of active sites in real fuel cells.

Acknowledgements

The authors acknowledge financial support from the Engineering and Physical Sciences Research Council (EPSRC) (EP/M013812/1, and EP/S023259/1), the European Research Council (ERC) under the European Union's Horizon 2020 research and innovation programme (grant agreement no. 866402) and the National Research Council of Canada through the Materials for Clean Fuels Challenge Program. A. P. thanks the EPSRC Centre for Doctoral Training in the Advanced Characterisation of Materials (grant number EP/L015277/1) and the Imperial College London SPIN-Lab (equipment grant number: EP/P030548/1), with measurements supported by Dr. Irena Nevjestic. A. L. acknowledges Marie Skłodowska- Curie Fellowship H2020-MSCA-IF-2019 (892614) through the project HAEMOGLOBIN. S. Ch. S. acknowledges Marie Skłodowska-Curie Fellowship H2020-MSCA-IF-2019 (896637). M.-M. Titirici acknowledges the Royal Academy of Engineering Chair in Emerging Technologies Fellowship. We would like to thank Dr Hossein Yadegari, Simon Kellner, and Yingqi Xu for assistance with materials characterization. A. B. acknowledges support from the Carlsberg foundation (grant number CF21-0114). R.G.S. thanks the Agence Nationale de la Recherche (Labex ARCANE, CBH-EUR-GS, ANR-17-EURE-0003).

References

[1] R. Jasinski, *Nature* **1964**, *201*, 1212.

[2] L. Du, V. Prabhakaran, X. Xie, S. Park, Y. Wang, Y. Shao, *Adv. Mater.* **2021**, *33*, 1908232.

[3] M. Lefèvre, E. Proietti, F. Jaouen, J.-P. Dodelet, *Science (80-.).* **2009**, *324*, 71 LP.

[4] M. Primbs, Y. Sun, A. Roy, D. Malko, A. Mehmood, M.-T. Sougrati, P.-Y. Blanchard, G. Granozzi, T. Kosmala, G. Daniel, P. Atanassov, J. Sharman, C. Durante, A. Kucernak, D. Jones, F. Jaouen, P. Strasser, *Energy Environ. Sci.* **2020**, *13*, 2480.

[5] G. Wu, K. L. More, C. M. Johnston, P. Zelenay, *Science (80-.).* **2011**, *332*, 443 LP.

[6] M. Titirici, S. G. Baird, T. D. Sparks, S. M. Yang, A. Brandt-Talbot, O. Hosseinaei, D. P. Harper, R. M. Parker, S. Vignolini, L. A. Berglund, Y. Li, H.-L. Gao, L.-B. Mao, S.-H. Yu, N. Díez, G. A. Ferrero, M. Sevilla, P. Á. Szilágyi, C. J. Stubbs, J. C. Worch, Y. Huang, C. K. Luscombe, K.-Y. Lee, H. Luo, M. J. Platts, D. Tiwari, D. Kovalevskiy, D. J. Fermin, H. Au, H. Alptekin, M. Crespo-Ribadeneyra, V. P. Ting, T.-P. Fellinger, J. Barrio, O. Westhead, C. Roy, I. E. L. Stephens, S. A. Nicolae, S. C. Sarma, R. P. Oates, C.-G. Wang, Z. Li, X. J. Loh, R. J. Myers, N. Heeren, A. Grégoire, C. Périssé, X. Zhao, Y. Vodovotz, B. Earley, G. Finnveden, A. Björklund, G. D. J. Harper, A. Walton, P. A. Anderson, *J. Phys. Mater.* **2022**, *5*, 032001.

[7] A. Pedersen, J. Barrio, A. Li, R. Jervis, D. J. L. Brett, M. M. Titirici, I. E. L. Stephens, *Adv. Energy Mater.* **2022**, *12*, 2102715.

[8] J. Wang, Z. Huang, W. Liu, C. Chang, H. Tang, Z. Li, W. Chen, C. Jia, T. Yao, S. Wei, Y. Wu, Y. Li, *J. Am. Chem. Soc.* **2017**, *139*, 17281.

[9] L. Ni, C. Gallenkamp, S. Paul, M. Kübler, P. Theis, S. Chabbra, K. Hofmann, E. Bill, A. Schnegg, B. Albert, V. Krewald, U. I. Kramm, *Adv. Energy Sustain. Res.* **2021**, *2*, 2000064.

[10] J. Li, M. T. Sougrati, A. Zitolo, J. M. Ablett, I. C. Oğuz, T. Mineva, I. Matanovic, P. Atanassov, Y. Huang, I. Zenyuk, A. Di Cicco, K. Kumar, L. Dubau, F. Maillard, G. Dražić, F. Jaouen, *Nat. Catal.* **2021**, *4*, 10.

[11] J. Barrio, A. Pedersen, S. Favero, H. Luo, M. Wang, S. C. Sarma, J. Feng, L. T. T. Ngoc, S. Kellner, A. Y. Li, A. B. Jorge Sobrido, M.-M. Titirici, *Chem. Rev.* **2022**, DOI 10.1021/acs.chemrev.2c00429.

[12] S. Wagner, H. Auerbach, C. E. Tait, I. Martinaiou, S. C. N. Kumar, C. Kübel, I. Sergeev, H.-C. Wille, J. Behrends, J. A. Wolny, V. Schünemann, U. I. Kramm, *Angew. Chemie Int. Ed.* **2019**, *58*, 10486.

[13] C. Gallenkamp, U. I. Kramm, V. Krewald, *Chem. Commun.* **2021**, *57*, 859.

[14] P. Hutchison, P. S. Rice, R. E. Warburton, S. Raugei, S. Hammes-Schiffer, *J. Am. Chem. Soc.* **2022**, *144*, 16524.

[15] X. Yang, D. Xia, Y. Kang, H. Du, F. Kang, L. Gan, J. Li, *Adv. Sci.* **2020**, *7*, DOI 10.1002/advs.202000176.

[16] X. She, J. Gao, Y. Gao, H. Tang, K. Li, Y. Wang, Z. Wu, *New J. Chem.* **2022**, *46*, 16138.

[17] L. Jiao, J. Li, L. L. Richard, Q. Sun, T. Stracensky, E. Liu, M. T. Sougrati, Z. Zhao, F. Yang, S. Zhong, H. Xu, S. Mukerjee, Y. Huang, D. A. Cullen, J. H. Park, M. Ferrandon, D. J. Myers, F. Jaouen, Q. Jia, *Nat. Mater.* **2021**, *20*, 1385.

[18] A. Mehmood, M. Gong, F. Jaouen, A. Roy, A. Zitolo, A. Khan, M. Sougrati, M. Primbs, A. M. Bonastre, D. Fongalland, G. Drazic, P. Strasser, A. Kucernak, *Nat. Catal.* **2022**, *5*, 311.

[19] A. Mehmood, J. Pampel, G. Ali, H. Y. Ha, F. Ruiz-Zepeda, T.-P. Fellinger, *Adv. Energy Mater.* **2018**, *8*,

1701771.

[20] D. Menga, F. Ruiz-Zepeda, L. Moriau, M. Šala, F. Wagner, B. Koyutürk, M. Bele, U. Petek, N. Hodnik, M. Gaberšček, T. Fellinger, *Adv. Energy Mater.* **2019**, *9*, 1902412.

[21] R. Van Hardeveld, F. Hartog, *Surf. Sci.* **1969**, *15*, 189.

[22] F. Jaouen, D. Jones, N. Coutard, V. Artero, P. Strasser, A. Kucernak, *Johnson Matthey Technol. Rev.* **2018**, *62*, 231.

[23] A. M. Damjanović, B. Koyutürk, Y.-S. Li, D. Menga, C. Eickes, H. A. El-Sayed, H. A. Gasteiger, T.-P. Fellinger, M. Piana, *J. Electrochem. Soc.* **2021**, *168*, 114518.

[24] T. A. M. Suter, K. Smith, J. Hack, L. Rasha, Z. Rana, G. M. A. Angel, P. R. Shearing, T. S. Miller, D. J. L. Brett, *Adv. Energy Mater.* **2021**, *11*, 2101025.

[25] H. A. Gasteiger, S. S. Kocha, B. Sompalli, F. T. Wagner, *Appl. Catal. B Environ.* **2005**, *56*, 9.

[26] N. R. Sahraie, U. I. Kramm, J. Steinberg, Y. Zhang, A. Thomas, T. Reier, J.-P. Paraknowitsch, P. Strasser, *Nat. Commun.* **2015**, *6*, 8618.

[27] X. Wan, X. Liu, Y. Li, R. Yu, L. Zheng, W. Yan, H. Wang, M. Xu, J. Shui, *Nat. Catal.* **2019**, *2*, 259.

[28] M. Primbs, Y. Sun, A. Roy, D. Malko, A. Mehmood, M.-T. Sougrati, P.-Y. Blanchard, G. Granozzi, T. Kosmala, G. Daniel, P. Atanassov, J. Sharman, C. Durante, A. Kucernak, D. Jones, F. Jaouen, P. Strasser, *Energy Environ. Sci.* **2020**, *13*, 2480.

[29] S. Ma, G. A. Goenaga, A. V Call, D. Liu, *Chem. Eur. J.* **2011**, *17*, 2063.

[30] E. Proietti, F. Jaouen, M. Lefèvre, N. Larouche, J. Tian, J. Herranz, J.-P. Dodelet, *Nat. Commun.* **2011**, *2*, 1.

[31] S. Pylypenko, S. Mukherjee, T. S. Olson, P. Atanassov, *Electrochim. Acta* **2008**, *53*, 7875.

[32] J. Barrio, A. Pedersen, J. Feng, S. C. Sarma, M. Wang, A. Y. Li, H. Yadegari, H. Luo, M. P. Ryan, M.-M. Titirici, I. E. L. Stephens, *J. Mater. Chem. A* **2022**, *10*, 6023.

[33] C. Wei, R. R. Rao, J. Peng, B. Huang, I. E. L. Stephens, M. Risch, Z. J. Xu, Y. Shao-Horn, *Adv. Mater.* **2019**, *31*, 1806296.

[34] R. Zhou, Y. Zheng, M. Jaroniec, S.-Z. Qiao, *ACS Catal.* **2016**, *6*, 4720.

[35] D. Malko, A. Kucernak, T. Lopes, *Nat. Commun.* **2016**, *7*, 13285.

[36] M. K. Bhunia, K. Yamauchi, K. Takanabe, *Angew. Chemie Int. Ed.* **2014**, *53*, 11001.

[37] M. Shunmughanathan, N. Madankumar, K. Pitchumani, *ChemistrySelect* **2018**, *3*, 13743.

[38] Z. Zhou, F. He, Y. Shen, X. Chen, Y. Yang, S. Liu, T. Mori, Y. Zhang, *Chem. Commun.* **2017**, *53*, 2044.

[39] J. Barrio, M. Volokh, M. Shalom, *J. Mater. Chem. A* **2020**, *8*, 11075.

[40] Z. Chen, S. Pronkin, T.-P. Fellinger, K. Kailasam, G. Vilé, D. Albani, F. Krumeich, R. Leary, J. Barnard, J. Meurig Thomas, J. Pérez-Ramírez, M. Antonietti, D. Dontsova, *ACS Nano* **2016**, *10*, 3166.

[41] S. K. Kaiser, Z. Chen, D. Faust Akl, S. Mitchell, J. Pérez-Ramírez, *Chem. Rev.* **2020**, *120*, 11703.

[42] F. K. Kessler, Y. Zheng, D. Schwarz, C. Merschjann, W. Schnick, X. Wang, M. J. Bojdys, *Nat. Rev. Mater.* **2017**, *2*, 17030.

[43] B. Jürgens, E. Irran, J. Senker, P. Kroll, H. Müller, W. Schnick, *J. Am. Chem. Soc.* **2003**, *125*, 10288.

[44] W. Zhang, J. Barrio, C. Gervais, A. Kocjan, A. Yu, X. Wang, M. Shalom, *Angew. Chemie Int. Ed.* **2018**, *57*, 9764.

[45] J. Pampel, A. Mehmood, M. Antonietti, T.-P. Fellinger, *Mater. Horizons* **2017**, *4*, 493.

[46] H. May, *J. Appl. Chem.* **1959**, *9*, 340.

[47] S. C. Moldoveanu, *Pyrolysis of Organic Molecules: Applications to Health and Environmental Issues*, Elsevier, **2009**.

[48] C. Hu, F. Chen, Y. Wang, N. Tian, T. Ma, Y. Zhang, H. Huang, *Adv. Mater.* **2021**, *33*, 2101751.

[49] J. Zhang, F. Bi, J. Zhang, X. Wang, Z. Yang, G. Zhang, B. Wang, *RSC Adv.* **2021**, *11*, 288.

[50] J. Mahmood, E. K. Lee, M. Jung, D. Shin, I.-Y. Jeon, S.-M. Jung, H.-J. Choi, J.-M. Seo, S.-Y. Bae, S.-D. Sohn, N. Park, J. H. Oh, H.-J. Shin, J.-B. Baek, *Nat. Commun.* **2015**, *6*, 6486.

[51] B. Németh, C. Wéber, T. Veszprémi, T. Gáti, Á. Demeter, *J. Org. Chem.* **2006**, *71*, 4910.

[52] B. V. Lotsch, M. Döblinger, J. Sehnert, L. Seyfarth, J. Senker, O. Oeckler, W. Schnick, *Chem. – A Eur. J.* **2007**, *13*, 4969.

[53] M. Mazzucato, G. Daniel, A. Mehmood, T. Kosmala, G. Granozzi, A. Kucernak, C. Durante, *Appl. Catal. B Environ.* **2021**, *291*, 120068.

[54] D. Menga, J. L. Low, Y.-S. Li, I. Arčon, B. Koyutürk, F. Wagner, F. Ruiz-Zepeda, M. Gaberšček, B. Paulus, T.-P. Fellinger, *J. Am. Chem. Soc.* **2021**, *143*, 18010.

[55] N. A. Zhuk, V. P. Lutoev, B. A. Makeev, S. V. Nekipelov, A. V. Koroleva, A. V. Fedorova, M. V. Yermolina, D. S. Beznosikov, L. O. Karlova, *J. Mater. Res. Technol.* **2020**, *9*, 4173.

[56] J. Nehrkorn, B. M. Martins, K. Holldack, S. Stoll, H. Dobbek, R. Bittl, A. Schnegg, *Mol. Phys.* **2013**, *111*, 2696.

[57] S. Kamali-M., T. Ericsson, R. Wäppling, *Thin Solid Films* **2006**, *515*, 721.

[58] T. Mineva, I. Matanovic, P. Atanassov, M. T. Sougrati, L. Stievano, M. Clémancey, A. Kochem, J. M. Latour, F. Jaouen, *ACS Catal.* **2019**, *9*, 9359.

[59] C. H. Choi, H. K. Lim, M. W. Chung, G. Chon, N. Ranjbar Sahraie, A. Altin, M. T. Sougrati, L. Stievano, H. S. Oh, E. S. Park, F. Luo, P. Strasser, G. Dražić, K. J. J. Mayrhofer, H. Kim, F. Jaouen, *Energy Environ. Sci.* **2018**, *11*, 3176.

[60] C. H. Choi, C. Baldizzone, J. P. Grote, A. K. Schuppert, F. Jaouen, K. J. J. Mayrhofer, *Angew. Chemie - Int. Ed.* **2015**, *54*, 12753.

[61] A. Zitolo, V. Goellner, V. Armel, M. T. Sougrati, T. Mineva, L. Stievano, E. Fonda, F. Jaouen, *Nat. Mater.* **2015**, *14*, 937.

[62] D. Malko, T. Lopes, E. Symianakis, A. R. Kucernak, *J. Mater. Chem. A* **2015**, *4*, 142.

[63] A. Mehmood, M. Gong, F. Jaouen, A. Roy, A. Zitolo, A. Khan, M. Sougrati, M. Primbs, A. M. Bonastre, D. Fongalland, G. Drazic, P. Strasser, A. Kucernak, *Nat. Catal.* **2022**, *5*, 311.

[64] F. Luo, S. Wagner, W. Ju, M. Primbs, S. Li, H. Wang, U. I. Kramm, P. Strasser, *J. Am. Chem. Soc.* **2022**, *144*, 13487.

[65] K. Kumar, T. Asset, X. Li, Y. Liu, X. Yan, Y. Chen, M. Mermoux, X. Pan, P. Atanassov, F. Maillard, L. Dubau, *ACS Catal.* **2021**, *11*, 484.

[66] K. Kumar, L. Dubau, M. Mermoux, J. Li, A. Zitolo, J. Nelayah, F. Jaouen, F. Maillard, *Angew. Chemie Int. Ed.* **2020**, *59*, 3235.

[67] Q. Wang, Y. Yang, F. Sun, G. Chen, J. Wang, L. Peng, W. Chen, L. Shang, J. Zhao, D. Sun-Waterhouse, T. Zhang, G. I. N. Waterhouse, *Adv. Energy Mater.* **2021**, *11*, 2100219.

[68] G. Chen, Y. An, S. Liu, F. Sun, H. Qi, H. Wu, Y. He, P. Liu, R. Shi, J. Zhang, A. Kuc, U. Kaiser, T.

Zhang, T. Heine, G. Wu, X. Feng, *Energy Environ. Sci.* **2022**, *15*, 2619.

[69] D. H. Kim, S. Ringe, H. Kim, S. Kim, B. Kim, G. Bae, H.-S. Oh, F. Jaouen, W. Kim, H. Kim, C. H. Choi, *Nat. Commun.* **2021**, *12*, 1856.

[70] D. Malko, A. Kucernak, T. Lopes, *J. Am. Chem. Soc.* **2016**, *138*, 16056.

[71] F. Luo, A. Roy, L. Silvioli, D. A. Cullen, A. Zitolo, M. T. Sougrati, I. C. Oguz, T. Mineva, D. Teschner, S. Wagner, J. Wen, F. Dionigi, U. I. Kramm, J. Rossmeisl, F. Jaouen, P. Strasser, *Nat. Mater.* **2020**, *19*, 1215.

[72] F. Calle-Vallejo, A. Krabbe, J. M. García-Lastra, *Chem. Sci.* **2017**, *8*, 124.

[73] J. K. Nørskov, J. Rossmeisl, A. Logadottir, L. Lindqvist, J. R. Kitchin, T. Bligaard, H. Jónsson, *J. Phys. Chem. B* **2004**, *108*, 17886.

[74] D. Menga, A. Guilherme Buzanich, F. Wagner, T.-P. Fellinger, *Angew. Chemie Int. Ed.* **2022**, *n/a*, e202207089.